Journal of Power Sources 462 (2020) 228186

Contents lists available at ScienceDirect

Journal of Power Sources

journal homepage: www.elsevier.com/locate/jpowsour

Advanced electrochemical investigations of niobium modified $Li_2ZnTi_3O_8$ lithium ion battery anode materials

Naila Firdous [a,b], Nasima Arshad [a,*], Søren Bredmose Simonsen [b], Prasanna Kadirvelayutham [b], Poul Norby [b,**]

[a] Department of Chemistry, Allama Iqbal Open University Islamabad, 44000, Pakistan
[b] Department of Energy Conversion and Storage, Technical University of Denmark, Frederiksborgvej 399, P.O. Box 49, Roskilde, DK-4000, Denmark

HIGHLIGHTS

- Facile solid-state synthesis of Nb-doped $Li_2ZnTi_3O_8$.
- Structure, stability of $Li_2ZnTi_{2.95}Nb_{0.05}O_8$ by SAED TEM & *in-situ* XRD.
- Low R_{ct} & highest reversibility, discharge capacity of LZTNO-05.
- LZTNO-05 as potential anode electrode for Li-ion batteries.

GRAPHICAL ABSTRACT

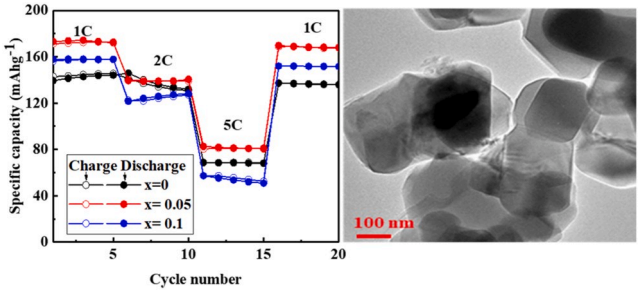

ARTICLE INFO

Keywords:
Doping
Lithium ion battery
Anode material
Agglomeration
Ball milling

ABSTRACT

$Li_2ZnTi_{3-x}Nb_xO_8$ (x = 0, 0.05, 0.1) (LZTNO) materials are synthesized through ball milling assisted solid state synthesis and its structural, morphological and electrochemical investigations are carried out. All LZTNO samples exhibit a spinel type structure with space group $P4_332$ and small amounts of anatase TiO_2 are also found in doped samples. The structure and mechanism of electrochemical reaction of $Li_2ZnTi_3O_8$ (LZTO) is not changed or disturbed significantly with the introduction of small amount of Nb^{+5} dopant. All samples show a uniform size distribution but $Li_2ZnTi_{2.95}Nb_{0.05}O_8$ (LZTNO-05) displays less agglomeration and more uniform size distribution. Also, the LZTNO-05 sample exhibit low charge transfer resistance and higher reversibility. Galvanostatic charge-discharge reveals highest discharge capacities of 223.9, 211, 173.7, 140, 83.7 mA h g^{-1} of LZTNO-05 at different C-rates 0.1C, 0.2C, 1C, 2C, and 5C, respectively. Pristine LZTO shows smaller discharge capacities of 197, 184, 146, 129.8 and 68.9 mA h g^{-1} at 0.1C, 0.2C, 1C, 2C and 5C rates, respectively. LZTNO-05 is prepared by a cost-effective route with excellent electrochemical properties making it more attractive as potential anode electrode for commercialization.

* Corresponding author.
** Corresponding author.
E-mail addresses: nasimaa2006@yahoo.com, nasima.arshad@aiou.edu.pk (N. Arshad), pnor@dtu.dk (P. Norby).

https://doi.org/10.1016/j.jpowsour.2020.228186
Received 19 December 2019; Received in revised form 18 March 2020; Accepted 12 April 2020
Available online 21 April 2020

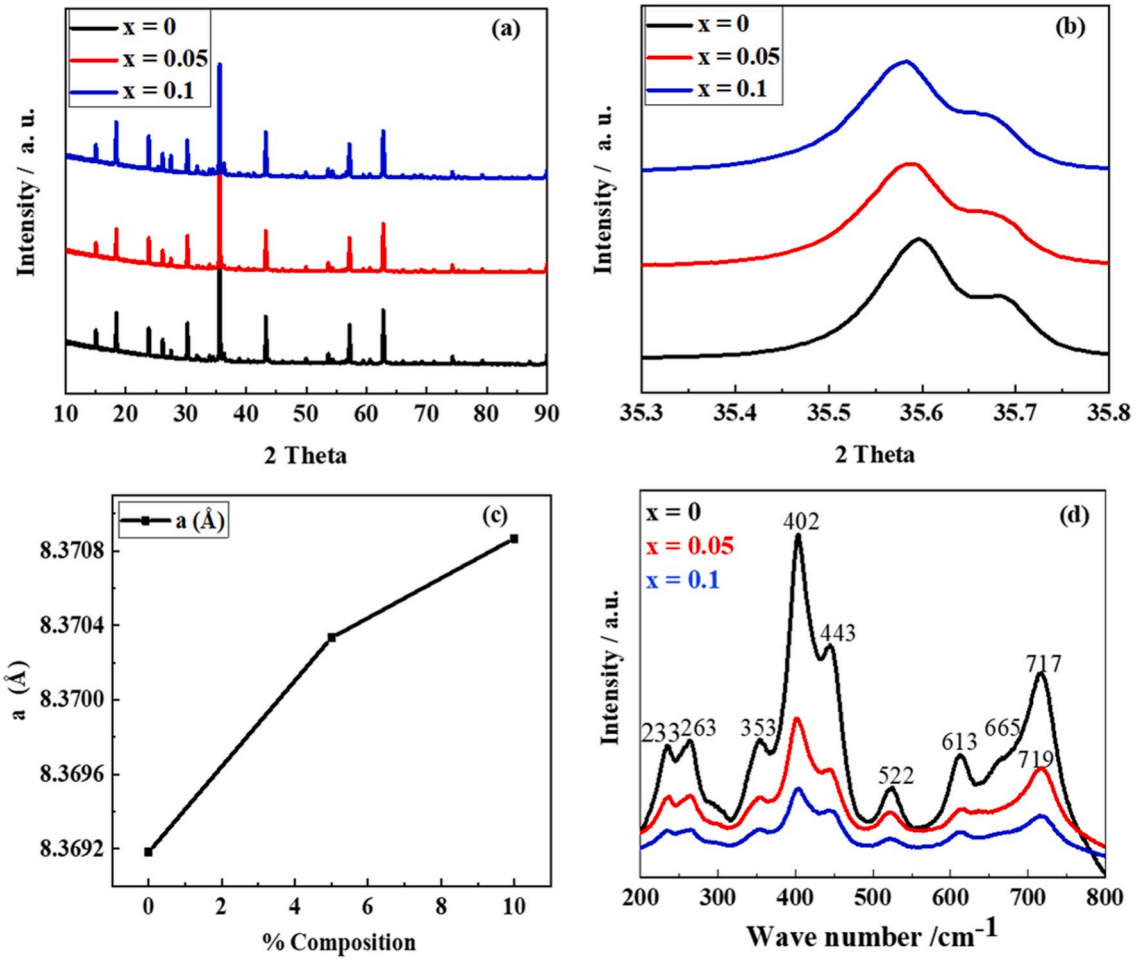

Fig. 1. (a) XRD pattern (b) enlarged (311) diffraction peak, (c) Unit cell parameter a (Å) on the basis of Rietveld refinement and (d) Raman spectra of LZTNO.

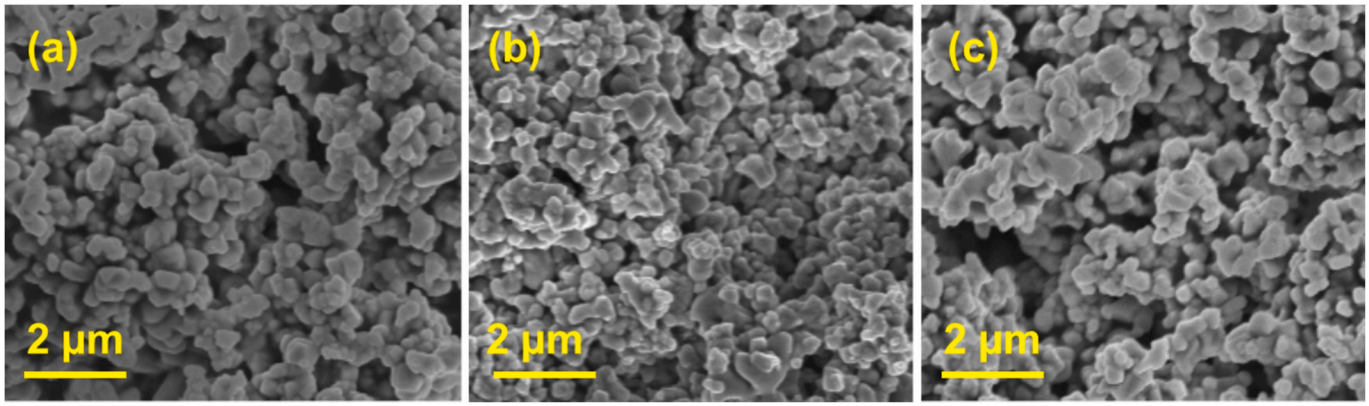

Fig. 2. SEM images of LZTNO (a) x = 0, (b) x = 0.05, (c) x = 0.1.

1. Introduction

In order to satisfy environment protection issue and to combat increased energy demand to ensure sustainable development of the world it is vital to develop renewable and clean energy systems. For this purpose, in 1990 Sony introduced lithium ion batteries (LIBs). In portable electric devices, hybrid electric vehicles (HEVs), Plug in hybrid electric vehicles (PHEVs), electric vehicles (EVs) lithium ion batteries are used as a promising technology due to small volume changes, long cycle life, high energy density, light weight, no memory effect and high voltage [1]. In commercial lithium ion batteries graphite is used as anode which has high capacity (372 mA h g^{-1}), is inexpensive, have high specific capacity and is chemically inert. Graphite containing anode materials intercalate lithium at very low potential close to lithium plating which causes growth of lithium dendrites which is a safety risk and as a result short circuiting of batteries can take place. So, there is a continuous investigation for alternative materials which have high safety and cost effectiveness. Titanium based materials offer such properties i.e. safety and stability [2–6]. Researchers are interested in developing new anode materials for lithium ion batteries due to the

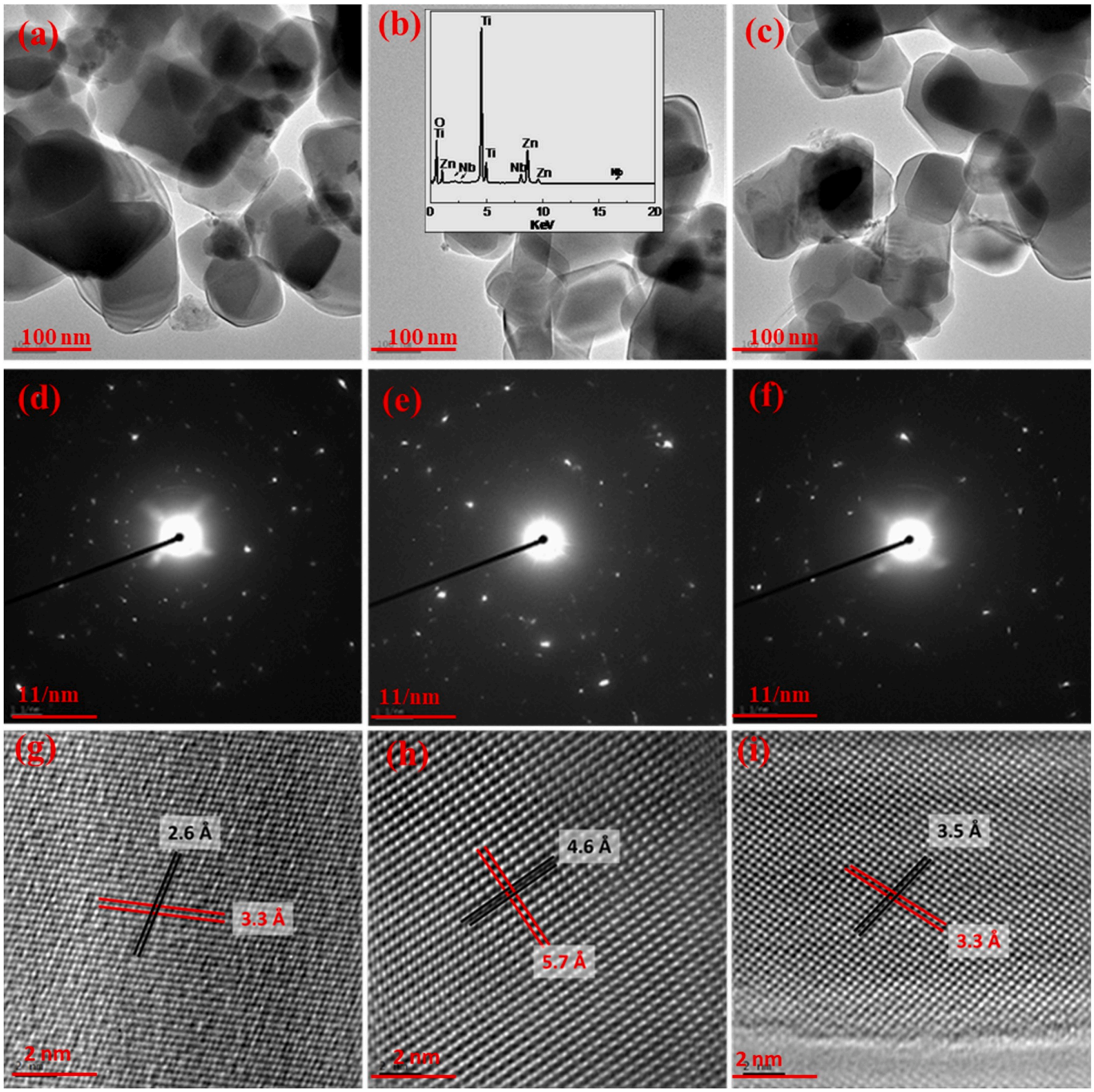

Fig. 3. (a–c) TEM images, (d–f) SAED pattern and (g–i) HRTEM images are presented for LZTNO, x = 0 (a,d,g), 0.05 (b,e,h), 0.1 (c,f,i). Measured lattice distances are indicated at the HRTEM images.

increased demand of energy density and power density for lithium ion batteries. Recently a titanium containing class of compounds $Li_2MTi_3O_8$ (M = Ni, Zn, Mg, Co) attracted attention due to its higher theoretical capacity and stability [5,7,8]. Introduction of Zn in the cubic spinel type structure ($Li_2ZnTi_3O_8$) results in a two-step discharge process with voltage plateaus at ~1 V and ~0.5 V and a charge plateau at ~1.5 V. The material shows good thermal and structural stability also in full cells [9–14]. Three Ti^{4+} are present in the structure of LZTO, so according to theoretical studies they can be converted to $3Ti^{3+}$ and the material will offer a theoretical capacity of 227 mA h g^{-1} [15]. The LZTO insertion and de-insertion, the reaction can be shown in the following equation [16].

$$Li_2ZnTi_3O_8 + 3Li^+ + 3e^- \rightarrow Li_5ZnTi_3O_8$$

Structural reports of LZTO reveal that its space group is $P4_332$ and its cell parameters are $a = b = c = 8.35596(2)$ Å [17].

However, LZTO exhibits low conductivity and the lithium diffusion coefficient is also low due to which its practical applications are limited. These properties can be enhanced by formulation with other conductive phases, designing different morphology [18,19], surface modification by coating [20–22], doping and nanosizing [19]. Doping with elements like Ce^{+4} [23], V^{+5} [24], Fe^{+3} [25], Cu^{+2} [26], Mo^{+6} [27], Zr^{+4} [20], Ag^{+1} [28], Na^+ [17] and Ti^{+3} [29] resulted in enhanced electrochemical performance of LZTO. Selection of a suitable element for doping has a significant role in order to improve overall performance of an electrode

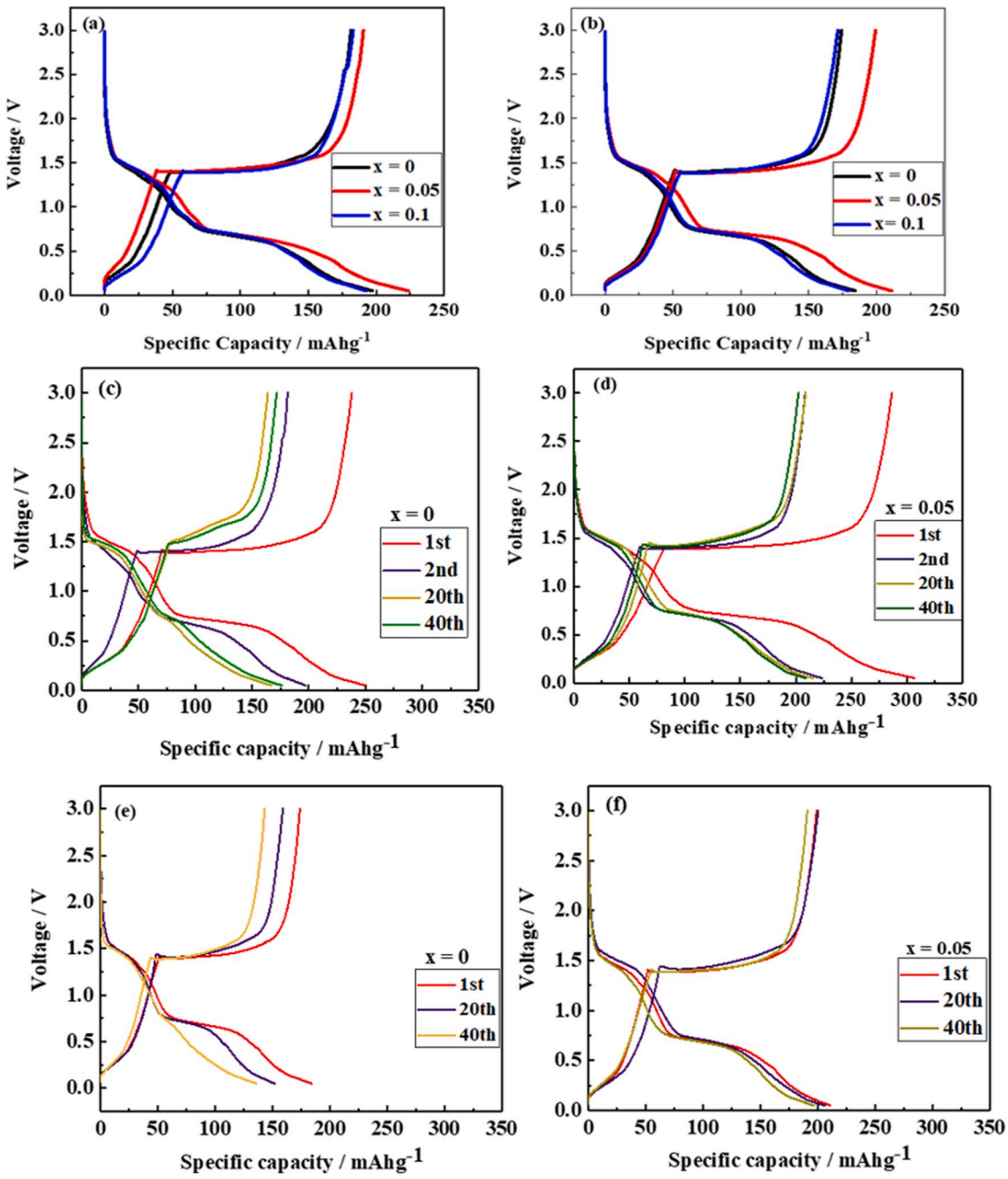

Fig. 4. Charge-discharge curves of LZTNO at (a,c & d) 0.1C and (b,e & f) 0.2C.

material. In order to improve the electronic conductivity of titanium-based materials doping with high valence ions like Nb^{+5} is very effective also to stabilize their structure. Selection of niobium is principally based on the fact that ionic radius of Nb^{+5} and Ti^{+4} are very close so this substitution will not very difficult, secondly introduction of Nb^{+5} in crystal lattice of LZTO can increase its electronic conductivity significantly by increasing concentration of electrons. It also improves the cyclic performance and capacity [30]. LZTO can be synthesized by many synthetic methods i.e., solid state synthesis [31], molten salt method [15], sol gel synthesis [4,32–34] etc. The present research is focused on cost effective ball milling assisted solid state synthesis of LZTO and its Nb^{+5} doped analogues for fast charging discharging and as a potential candidate for commercial lithium ion batteries [20].

2. Experimental

2.1. Materials and synthesis

Ball milling assisted solid-state method is used to synthesize (Li_2Z-$nTi_{3-x}Nb_xO_8$, x = 0, 0.05, 0.1). A stoichiometric amount of following raw materials was taken anatase TiO_2 (Aldrich 99.8%), $Zn(CH_3COO)_2{\cdot}2H_2O$ (Fluka 99%), Li_2CO_3 (Alfa Aesar 99%) and Nb_2O_5 (Sigma Aldrich 99.9%). All raw materials are mixed, and ball milled in ethanol for 3 h at a speed of 100 rpm and the resulting mixture was dried overnight in an oven at 120 °C in air. The obtained material was ground and sintered for 6 h at 800 °C with a ramp rate of 3 °C per minute, cooled to room temperature then the powder was again ground with pestle and mortar to get LZTNO (x = 0, 0.05, 0.1) final powders.

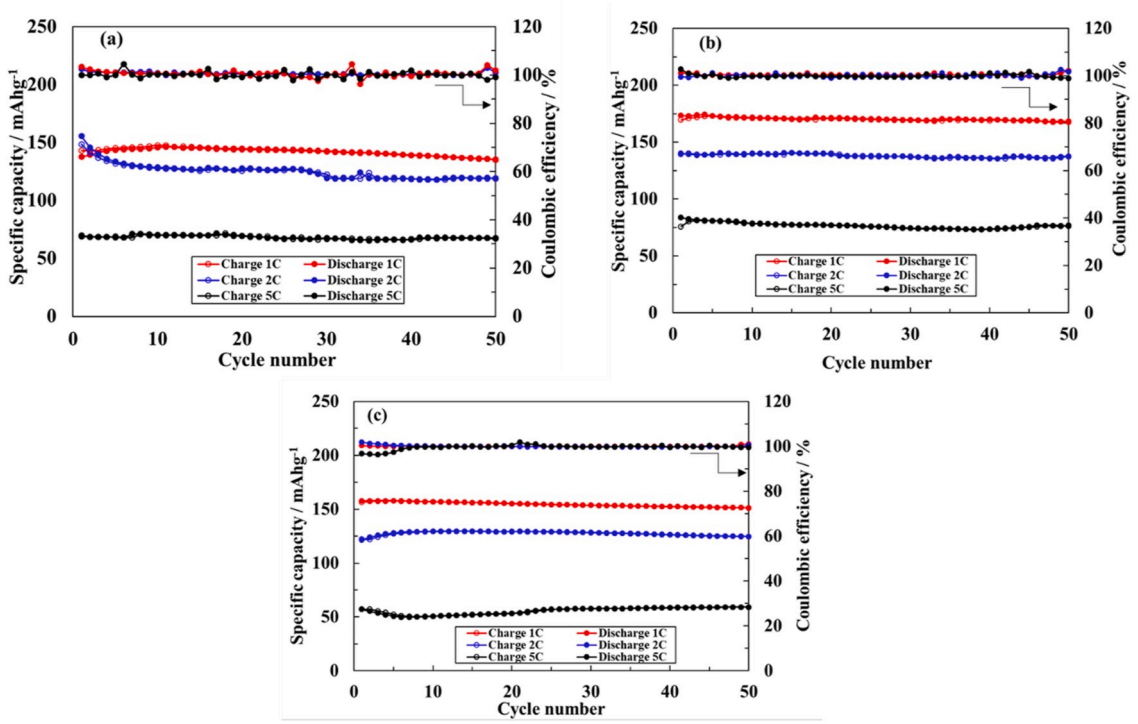

Fig. 5. Cycling properties and coulombic efficiencies of LZTNO (a) x = 0, (b) x = 0.05 and (c) x = 0.1 respectively.

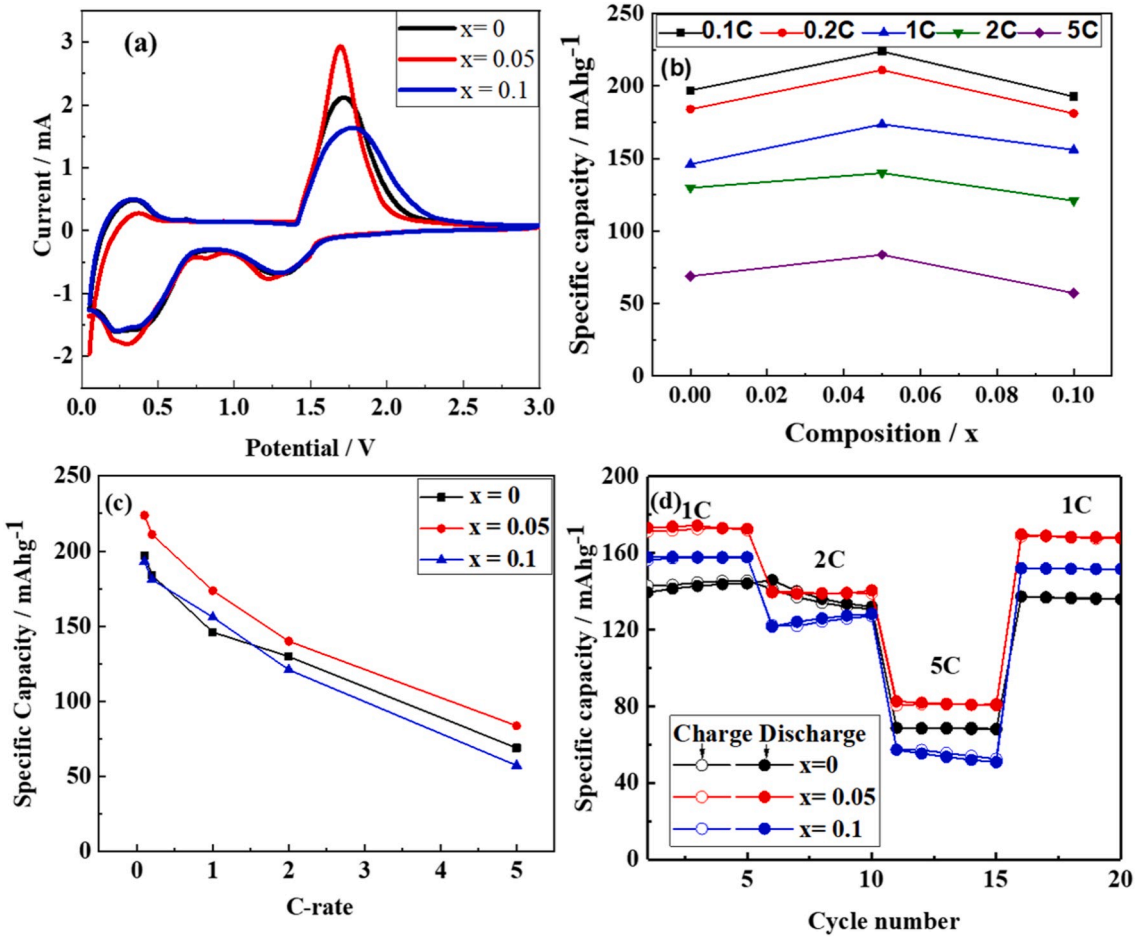

Fig. 6. (a) Cyclic voltammetry (CV) curves (b) Rate performance (c) Dependence of specific capacity on C-rate (d) Cycling performance of LZTNO materials at different rates.

Table 1
Electrochemical parameters (potential difference between anodic and cathodic peaks from CV and fitting data from EIS patterns).

Sample	φ_{Pa} (V)	φ_{Pc}(V)	$\Delta\varphi_{P}$(mV)	Rs (Ω)	R_{ct} (Ω)
LZTO	1.726	1.227	499	6.522	115.3
LZTNO-05	1.696	1.222	474	10.31	77.86
LZTNO-1	1.761	1.227	534	3.317	87.91

2.2. Electrode preparation

Electrode slurries were prepared by mixing the active material, super P conductive carbon (Timcal C65) and polyvinylidene fluoride (PVDF Kynar) as a binder with 80:10:10 wt% ratio and dispersing it in N-methyl-2-pyrrolidone (NMP Sigma Aldrich 99.5%). The slurry was coated on copper foil with the help of doctor blade technique. The loading of active material was 3–3.5 mgcm^{-2}. The coating was dried and then roll pressed. Electrodes of 15 mm diameter were punched and dried overnight in a vacuum oven in the glove box. Coin cells CR2032 were assembled using lithium foil as counter and reference and the punched electrode on the copper foil as the working electrode. A 1 M solution of $LiPF_6$ in a 1:1 vol ratio ethylene carbonate (EC): dimethyl carbonate (DMC) was used as an electrolyte. The level of oxygen and water in the glove box was less than 0.1 ppm.

2.3. Physical characterization

Crystal structure studies and material identification was carried out using X-ray diffraction (XRD) on a Rigaku SmartLab diffractometer (Bragg Brentano geometry, Cu-Kα radiation, 10–90° in 2theta, step size 0.02° in 2theta). Rietveld refinement was performed using the FullProf software suite. For morphology studies and particle size analysis scanning electron microscopy (SEM Zeiss Ultra) was used. Raman spectroscopy was carried out at 532 nm laser excitation at ambient temperature with Raman spectrometer (Renishaw inVia Spectrometer). Transmission electron microscopy (TEM), selected area electron diffraction (SAED) and energy dispersive spectroscopy (EDS) were performed by using a JEOL 3000F equipped with a field emission gun operated at 300 kV and an Oxford instruments EDS detector. The specimens were prepared for TEM adding a dispersion of sample powders in ethanol to a standard TEM Cu grid with a holey carbon support film. Quantifications of the EDS spectra were performed with calculated k-factors from the INCA software. High-resolution TEM (HRTEM) images recorded analyzed with the Crystal Match software [35]. Here at least three independent measurements, two lattice distances and the angle between the planes were compared to theoretical values described in crystallographic information files (CIF). Crystals are found to be consistent with a structure of all three measurements agree with the theoretical values within estimated measurement errors of 10% for distances and 5% for angles.

2.4. Electrochemical measurements

Electrochemical measurements of LZTNO were performed using a Biologic VMP3 multi-channel potentiostat and data were analyzed using the ECLAB software. The measurements include cyclic voltammetry (CV) in the range of 0.05–3 V with scan rate 0.5 mV s^{-1}, electrochemical impedance spectroscopy (EIS) was carried out with AC amplitude of 5 mV in frequency range of 0.01 Hz–10 kHz and charging-discharging tests of cells at different C-rates in voltage range between 0.05 V and 3 V were carried out.

2.5. Preliminary in-situ diffraction studies

In-situ XRD experiments were performed on a Rigaku SmartLab diffractometer in reflection geometry using a modified EL-Cell (ECC-OPTO) *in-situ* battery cell. A 7 mm diameter pellet of LZTNO with a thickness of ca. 250 μm was pressed from scraped-off coated electrode material. The cell was assembled in a glovebox using a lithium foil as the negative electrode and the same electrolyte (1 M $LiPF_6$ in 1:1 EC/DMC) as for the electrochemical characterization. Diffraction data were collected from 10 to 130° in 2theta using a step size of 0.0152° in 2theta. The collection time for each XRD pattern was 32 min.

3. Results and discussion

3.1. Structure and morphology

The XRD pattern of the LZTNO samples is shown in Fig. 1(a). The main diffraction peaks of all materials match diffraction peaks of LZTO having space group $P4_332$ (JCPDS# 86_1512). In order to understand the crystal structure in detail Rietvield refinement was carried out, Fig. S1 (in the supplementary material). The refinements show that in this spinel structure 12d and 8b sites are occupied by Li and Ti, and Zn and Li share crystallographic 8c sites. However, in case of higher amount of niobium impurity peaks also appear which are attributed to anatase TiO_2. The amount of TiO_2 in the phases were estimated from Rietveld refinement: LZTO: 1.4 w%, LZTNO-05 2.8 w%, LZTNO-1: 5.7 w%.Here no niobium containing impurity phase appeared in the analysis which confirms that all the Nb^{+5} has entered into the crystal lattice of the doped LZTNO. By doping on titanium (Ti^{+}) site of LZTO with higher valence and larger Nb^{+5} ions reasonably its conductivity enhances because of an increase in electron concentration [36]. TiO_2 is also an active electrode material having fast insertion extraction and high insertion potential (2 V vs Li/Li^{+}) due to which it is also used as a composite with $Li_4Ti_5O_{12}$–TiO_2. The capacity of titanium-based electrode materials for lithium-ion batteries has been shown to improve in the presence of a small amount of TiO_2 [37,38]. $Li_2ZnTi_3O_8/TiO_2$ composite anode materials synthesized by co-precipitation showed

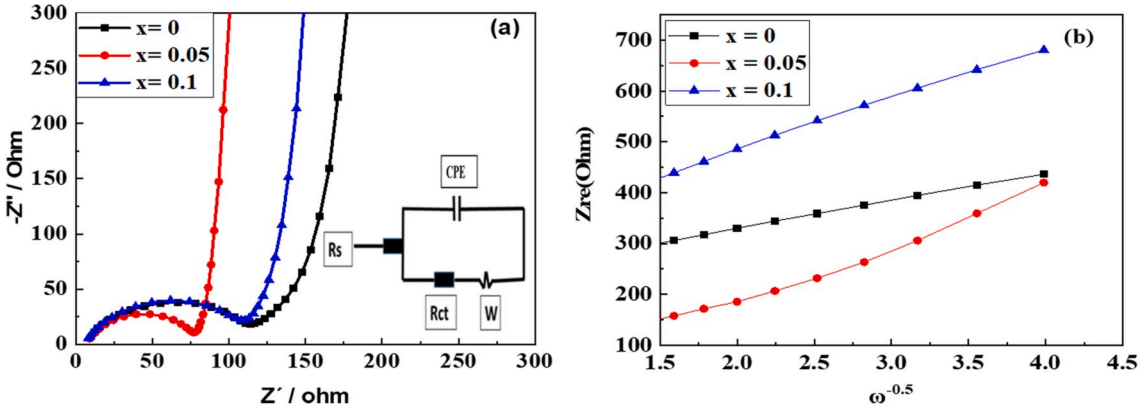

Fig. 7. (a) EIS curves of LZTNO materials (b) Graph of Z_{re} plotted against $\omega^{-1/2}$ at low-frequency region.

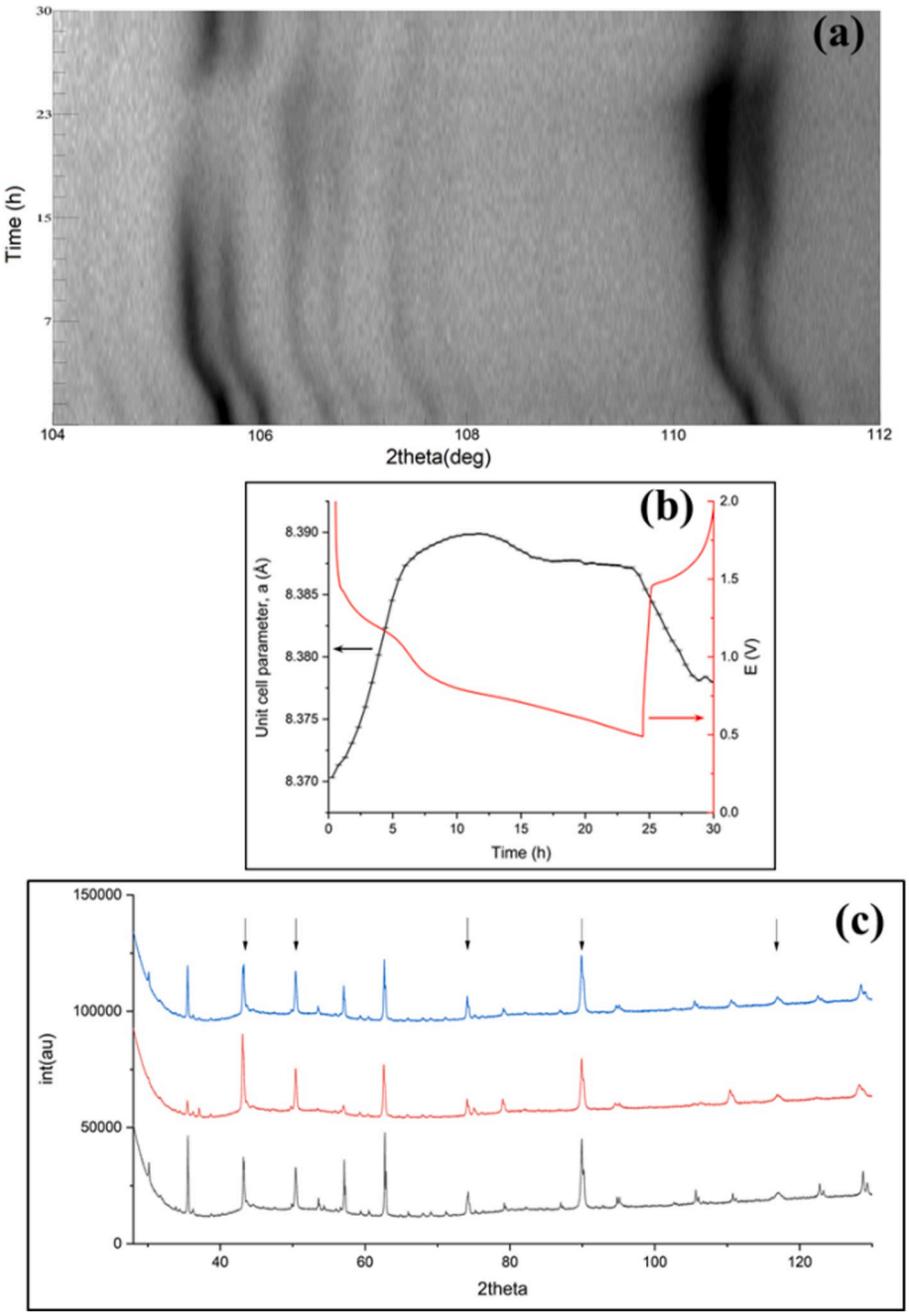

Fig. 8. (a) 2D representation of a part of the diffraction patterns during the first discharge/charge cycle of LZTNO-05. (b) Unit cell parameter (*a*-axis) during the first discharge/charge cycle of LZTNO-05 and the current during discharge was 50 μA and the voltage is shown in inset. (c) XRD patterns of LZTNO-05 at different charge/discharge state in the initial, charged and final state. The arrows indicate contributing reflections from the copper grid in the *in-situ* cell.

excellent cycling performance with high rate capacity [39]. This could partially explain the increase in capacity and cycling capability for LZTNO-05 where an appreciable amount of TiO_2 is present. In Fig. 1(b) the strongest diffraction peak (311) is enlarged to show the difference in peak position. The small shift in the peak position of the doped materials towards the lower angle reflects the change in lattice parameters. It indicated that the spinel structure of $Li_2ZnTi_3O_8$ did not change significantly with Nb-doping, but a slight increase in the cubic unit cell parameter with doping was observed Fig. 1(c). The values of lattice parameters are provided in Table S1(in the supplementary material). The change is small and may be due to the larger ionic radius of Nb^{+5} (0.64 Å) compared to Ti^{+4} (0.605 Å) or it may be a result of charge compensation reduction of some Ti^{+4} to Ti^{+3} (0.67 Å). In previous studies, it can be observed that when the niobium content is small than the decrease in lattice parameters appears because in this case, other parameters dominate [40–42]. But when the content of niobium exceeds 1% then the lattice parameters of doped materials increase as compared to pristine LZTO. Increment in the amount of niobium results in an increase in Ti^{+3} increasing electronic conductivity. Niobium content enhances the stability of the LZTNO during repeated insertion/deinsertion reaction of Li^+ because of the fact that the Nb–O bond is very stronger as compared to the Ti–O bond [43] .

Raman spectra of the LZTNO materials in the range of 200–800 cm^{-1} are shown in Fig. 1(d). Main peaks are observed at 233, 263, 353, 402, 443, 522, 613, 665, and 717 (719) cm^{-1}. LZTNO shows peak at 402 cm^{-1} due to vibrational mode of Zn–O symmetric stretching and Li–O

bonds of tetrahedral LiO_4 show stretching vibrations at 443 cm^{-1} [44]. Due to the A_1g mode of tetrahedral ZnO_4 strongest peak is observed at 402 cm^{-1} [45]. In the TiO_6 octahedral groups Ti–O bond shows a symmetric stretch at high-frequency band 717 cm^{-1} whereas in the case of doped materials a shift towards high frequency that is 719 cm^{-1} is observed because cation oxygen bonding is enhanced due to niobium doping [33]. Reports reveal that conductivity decrease with increased sharpness of A1g mode of compounds like $Li_xMn_2O_4$ ($0.1 < x < 2.0$) [46]. In the case of increased FWHM (full width half maximum) of A_1g mode, an increase of conductivity can be observed. Present studies of LZTNO-05 reveal an increase in FWHM (wider) as compared to (LZTO), so higher electronic conductivity can be expected from LZTNO-05.

SEM micrographs of the samples show no marked changes in the morphology of pristine and doped samples of LZTNO (x = 0, 0.05, 0.1) materials, Fig. 2. All the samples have irregular particles some of which aggregate together with no obvious difference in morphology under magnification of 2 μm. However, Nb doping has an obvious effect on the size distribution and as a result, LZTO possesses a wide particle size distribution and conspicuous agglomeration as compared to LZTNO-05 which is showing a narrow particle size distribution and less agglomeration [30]. In the crystal lattice of the LZTNO-05 presence of varied niobium prevents the overgrowth of crystals which results in decreased particle size through doping [47–49]. Nb doping results in narrow particle size distribution [50]. These micrographs show that sample with x = 0.05 shows good dispersion, uniform particle size, and less agglomeration as compared to the other samples. Maybe it could result in adequate contact between the electrode and electrolyte resulting in easier Li^+ diffusion and electron transport.

Fig. 3 (a-c) presents representative TEM images of LZTNO x = 0, 0.05 and 0.1, respectively. According to the images, the particle morphologies are comparable for all three materials.

The presence of Ti, Zn, O, and Nb is confirmed with EDS, Fig. S2 (in the supplementary material), while energies of the characteristic peak from Li are too low to be measured with EDS. SAED results from LZTNO, x = 0 (d), 0.05 (e), 0.1 (f) are presented in Fig. 3(d–f). The patterns are consistent with relatively large crystal sizes as (as observed in a-c) since the typical ring pattern observed for powders is broken up into separated spots. Analysis of a rotational integral of the patterns shows consistency with the cubic LZTO (Space-group 212, P 4_3 3 2) for all three materials. Measurements from at least three HRTEM images of each material show that the observed crystal structures for all three materials are consistent with the crystal structure of LZTO (space group P 4_3 3 2). Examples of HRTEM images from LZTNO x = 0 (g), 0.05 (h), 0.1 (i) are presented in Fig. 3(g–i) where measured lattice distances are indicated. The three HRTEM images in Fig. 3(g–i) present different crystals with different orientations, but they all match LZTNO. Specifically (g) lattice 1 = 3.3 Å, lattice 2 = 2.6 Å, angle = 74°. This for example match hkl (211), hkl (12–2), zone axis {-453}, (h) lattice 1 = 5.7 Å, lattice 2 = 4.6 Å, angle = 90°. This for example match hkl (110), hkl (1–11), zone axis {1-1-2}, (i) lattice 1 = 3.5 Å, lattice 2 = 3.3 Å, angle = 78°. This for example match hkl (211), hkl (11–2), zone axis {-351}.

3.2. Electrochemical studies

Fig. 4(a and b) is showing initial charge and discharge capacities of LZTNO (x = 0, 0.05, 0.1) materials at 0.1C and 0.2C rates respectively at a potential between 0.05 V–3 V. The charge/discharge capacities of LZTO and LZTNO-05 at 0.1C and 0.2C for first, second, 20th and 40th cycle is represented in Fig. 4(c–f). It is obvious from Fig. 4(c and d) that the initial capacity for pristine and doped material during the first cycle is higher as compared to theoretical capacity. This phenomenon can be explained on the basis of the fact that on the surface of the electrode during the first cycle electrolyte is decomposed as a result of irreversible electrochemical reaction, here trapping of some inactive Li^+ causes formation of solid electrolyte interface (SEI) which is very dense and even film. Anode materials commonly exhibit this phenomenon [17, 51–54]. For the initial charge and discharge curves, two apparent plateaus at 1.42 V and 0.71 V are observed which gradually fade in successive cycles. These plateaus are corresponding to lithium intercalation/deintercalation [8,55]. Quite obvious capacity retention is shown by the LZTNO-05 material at all C- rates as compared to pristine LZTO. Decreases in charge/discharge capacity of LZTO is more rapid on subsequent cycling.

In Fig. 5 the cycling performance and coulombic efficiencies of LZTNO (x = 0, 0.05, 0.1) materials between 0.05 and 3 V is shown at 1C, 2C, and 5C. From this Figure, it is clear that the LZTNO-05 sample is showing higher lithium storage capacity as compared to other samples after 50 cycles at all C-rates. LZTNO-05 material is showing close to 100% coulombic efficiency at all C-rates. The difference between the discharge and charge plateau increases with increased C-rate (1C, 2C, and 5C) for all materials. The LZTNO-05 material shows higher charge and discharge capacities compared to LZTO and LZTNO-1 material at all C-rates (0.1, 0.2C,1C, 2C, and 5C), Table S2 (in the supplementary martial).

The electrochemical reaction mechanism for LZTNO (x = 0, 0.05, 0.1) was studied with the help of cyclic voltammetry. Studies were carried out at a scan rate of 0.5 mVs^{-1} and the potential range was 0.05–3 V Fig. 6(a). The anodic peak potential (φ_{Pa}), cathodic peak potential (φ_{Pc}) and the difference between anodic and cathodic peaks ($\Delta\varphi_P$) are given in Table 1.

All materials showed a pair of cathodic and anodic peaks in the range of 1–2 V which represents that a small amount of Nb-doping did not affect the mechanism of electrochemical oxidation-reduction reaction of LZTO. The oxidation peak which appeared up to 1.7 V is regarded as the Ti^{+3}/Ti^{+4} oxidation reaction as in the case of spinel $Li_4Ti_5O_{12}$ [56]. The difference in potential between cathodic and anodic peak represents the degree of polarization. The potential difference values of samples LZTNO (x = 0, 0.05, 0.1) between oxidation and reduction peaks are 499, 474 and 534 mV respectively (Table 1) showing that the potential difference between cathodic and anodic peak is smallest for LZTNO-05. This sample is showing higher diffusion of lithium-ion and less polarization between electrodes as compared to pristine and other samples. As a result, the reversibility and cyclic stability of the electrodes are improved by appropriate doping of LZTO. An enveloped broad peak at low voltage (below 0.05 V) is attributed to the amorphous phase that may be a quasi-rock-salt [44]. Fig. 6(b) shows the relationship between the amount of doping and the specific capacity at different C-rates. It is obvious from this data that LZTNO-05 is showing the highest capacity at all C-rates. Fig. 6(c) shows the relation between specific capacity and C-rate. From here it can be noticed that with increasing C-rate the specific capacity decreases and at all C-rates the LZTNO-05 material showed highest capacity as compared to other materials. Fig. 6(d) shows the cycling performance of LZTNO at various C-rates. These results confirmed that LZTNO-05 material have better rate properties and cycling performance.

In order to investigate Li^+ ion diffusion from inside to electrode's surface, its migration through surface films and charge transfer interface electrochemical impedance spectroscopy was used [57].

Nyquist plots of LZTNO samples are shown in Fig. 7(a). The semicircle in the high-frequency region indicates charge transfer resistance and in the low-frequency region, lithium-ion diffusion is represented by an inclined line. An equivalent circuit was fitted through Elchemea analytical, shown in the inset. If we take into account the demonstration of Randles equivalent circuit it represents charge transfer resistance, double layer capacitance, and electrolyte resistance. Data on the basis of fitting of an equivalent circuit of charge transfer resistance (R_{ct}) and Ohmic resistance (R_s) of the solution is also listed in Table 1. In Fig. 7(a), CPE represents a constant phase element that is used in electrical circuits to represent the behavior of double layer and W is the Warburg impedance [58], which is due to diffusion resistance.

The data indicates that the LZTNO-05 sample has less Ohmic and charge transfer resistance as compared to pristine LZTO and LZTNO-1

samples. An appropriate amount of Nb doping on Ti site resulted in decreasing Ohmic as well as charge transfer resistance between active material and electrolyte. During cycling, this material shows better electrochemical activity than un-doped. Li-ion diffusion can be calculated from the straight line obtained in the low-frequency region of EIS data using the following equations [2,52,59].

$$D_{Li}^{+} = \frac{1}{2}\left(\frac{RT}{n^{2F^2}AC_{Li}\,\sigma}\right)^2 \quad (1)$$

where, R is the general gas constant (8.314 J $mol^{-1}K^{-1}$), T is the absolute temperature (298 K), n is the number of electrons transferred in the half reaction of the redox couple, Faraday's constant is F (96,485 C mol^{-1}), the area of the electrode is A (1.77 cm^2), the Li-ion concentration in material is C_{Li}. From the slope of line Z_{re}–$\omega^{-1/2}$ we get the value of the Warburg factor σ Fig. 7(b).

The relationship between ω i.e. Warburg impedance and Z_{re} i.e. real part of the impedance is given in eq. (2).

$$Z_{re} = R_{ct} + R_s + \sigma\,\omega^{-1/2} \quad (2)$$

With the help of equations (1) and (2) the calculated value of lithium-ion diffusion coefficients LZTNO (x = 0, 0.05, 0.1) were 1.1×10^{-15}, 5.8×10^{-15} and 1.98×10^{-15} cm^2s^{-1} respectively. From these values, it can be inferred that diffusion of lithium ions in LZTNO-05 sample revealed a slight increase.

Preliminary *in-situ* X-ray diffraction data on LZTNO-05 were collected using a discharge/charge current of 50 μA. A discharge capacity of 1.2 mA h was obtained (ca. 300 mA h/g) for the first discharge but only a short charge step was possible, ca. 80 m.

Fig. 8(a) shows a high-angle section of the 2D diffraction patterns as a function of time, while the 3D representation of the diffraction pattern is provided as Fig. S3 (in the supplementary material). Changes in the unit cell parameter are clearly visible during discharge and charge. Using Rietveld refinement, the cubic unit cell parameter was determined for each scan. Fig. 8(b) shows the unit cell parameter during the *in-situ* experiment (uncertainties given are from the refinement program (Full Prof)) together with the corresponding discharge/charge curve. An expansion of the unit cell is observed during the first part of the discharge. However, a maximum is observed approximately halfway through the discharge and a small contraction of the unit cell is observed in the last part of the discharge process. XRD patterns of LZTNO-05 at different charge/discharge states in the initial, charged and final state are shown in Fig. 8(c). As seen from Fig. 8(a) and (c) and S3, significant changes in the intensities of diffraction peaks are observed. This could signify larger structural changes upon the intercalation of the lithium ions in the structure, either structural rearrangement or loss of some of the structural integrity of the material. The changes close to the fully discharged state are accompanied by a broadening of the diffraction lines, Fig. 8(a), which could be indicative of increasing strain or disorder in the structure. As can be seen also from Fig. 8(a) and Fig. S3, the structural changes accompanying the delithiation/lithiation process are reversible as the crystallinity and intensity distribution are recovered during charge.

4. Conclusions

Cubic spinel structured LZTNO were synthesized through ball milling assisted solid-state route which is a facile method. Ti^{4+} was partially substituted by Nb^{+5} without destroying the crystal structure and mechanism of the electrochemical reaction of LZTO. The electrochemical performance of the materials studied is dependent on the Nb-substitution degree with LZTNO-05 ($Li_2ZnTi_{2\cdot95}Nb_{0\cdot05}O_8$) as the best performing material. LZTNO-05 delivered the highest discharge capacity at different C-rates, the lowest interface resistance, best rate capability and cycle stability of the prepared materials. The results show that the discharge capacity of pristine LZTO material is much smaller than for LZTNO-05. This enhancement in cycling stability and rate capacity can be attributed to reduced electrode polarization, lessened charge transfer resistance and enhancement of lithium-ion diffusion coefficient. With a low cost and facile method, LZTO and its Nb^{+5} doped analogues are prepared which are promising electrode materials for lithium-ion batteries. Preliminary *in-situ* XRD experiments revealed interesting reversible structural changes during discharge/charge. However, further *in-situ* studies are needed in order to elucidate the structural changes during the discharge/charge processes.

Authors contribution

This research was a part of Ph.D. work of N. F. under the supervision of N.A. All the experimental work was carried out at the Department of Chemistry, Allama Iqbal Open University, Islamabad Pakistan and Department of Energy Conversion and Storage, DTU by N.F. P.N. supervised her research work at DTU. S.B.S. and P.K. helped N·F in TEM and electrochemical data analysis, respectively. N.F. finalized her manuscript under the guidance of N.A. and P.N. Correspondence for the manuscript with the journal was done by N.A.

Declaration of competing interest

The authors declare that they have no known competing financial interests or personal relationships that could have appeared to influence the work reported in this paper.

CRediT authorship contribution statement

Naila Firdous: Writing - original draft, Data curation, Funding acquisition, Investigation. **Nasima Arshad:** Conceptualization, Supervision, Project administration, Visualization, Writing - review & editing. **Søren Bredmose Simonsen:** Formal analysis. **Prasanna Kadirvelayutham:** Writing - review & editing. **Poul Norby:** Methodology, Project administration, Validation, Writing - review & editing.

Acknowledgments

Theauthors are thankful to the Higher Education Commission of Pakistan for providing the IRSIP scholarship. This work was also supported by the DTU Energy project: Valuable carbon products from waste biomass (grant number 49734 E-1).

Appendix A. Supplementary data

Supplementary data to this article can be found online at https://doi.org/10.1016/j.jpowsour.2020.228186.

References

[1] H. Li, Z. Wang, L. Chen, X. Huang, Adv. Mater. 21 (2009) 4593–4607.
[2] C.K. Lan, S.I. Chuang, Q. Bao, Y.T. Liao, J.-G. Duh, J. Power Sources 275 (2015) 660–667.
[3] K.S. Park, A. Benayad, D.J. Kang, S.G. Doo, J. Am. Chem. Soc. 130 (2008) 14930–14931.
[4] Y. Xu, Z. Hong, L. Xia, J. Yang, M. Wei, Electrochim. Acta 88 (2013) 74–78.
[5] Z. Hong, M. Wei, X. Ding, L. Jiang, K. Wei, Electrochem. Commun. 12 (2010) 720–723.
[6] J. Liu, C. Du, Z. Tang, Ionics 20 (2014) 1495–1500.
[7] J. Wang, H. Zhao, Y. Shen, Z. Du, X. Chen, Q. Xia, ChemPlusChem 78 (2013) 1530–1535.
[8] Z. Hong, X. Zheng, X. Ding, L. Jiang, M. Wei, K. Wei, Energy Environ. Sci. 4 (2011) 1886–1891.
[9] Z. Wen, X. Wang, S. Mao, Z. Bo, H. Kim, S. Cui, G. Lu, X. Feng, J. Chen, Adv. Mater. 24 (2012) 5610–5616.
[10] H. Tang, L. Zan, W. Mao, Z. Tang, J. Electroanal. Chem. 751 (2015) 57–64.
[11] E. Pohjalainen, J. Kallioinen, T. Kallio, J. Power Sources 279 (2015) 481–486.
[12] Y. Wang, A. Zhou, X. Dai, L. Feng, J. Li, J. Li, J. Power Sources 266 (2014) 114–120.
[13] H. Park, T. Song, H. Han, U. Paik, J. Power Sources 244 (2013) 726–730.
[14] X. Sun, P.V. Radovanovic, B. Cui, New J. Chem. 39 (2015) 38–63.

[15] B. Chen, C. Du, Y. Zhang, R. Sun, L. Zhou, L. Wang, Electrochim. Acta 159 (2015) 102–110.
[16] Y. Ren, P. Lu, X. Huang, J. Ding, H. Wang, RSC Adv. 6 (2016) 49298–49306.
[17] W. Chen, Z. Zhou, R. Wang, Z. Wu, H. Liang, L. Shao, J. Shu, Z. Wang, RSC Adv. 5 (2015) 49890–49898.
[18] X. Li, Q. Xiao, B. Liu, H. Lin, J. Zhao, J. Power Sources 273 (2015) 128–135.
[19] L. Wang, L. Wu, Z. Li, G. Lei, P. Zhang, Electrochim. Acta 56 (2011) 5343–5346.
[20] H. Yang, J. Park, C.S. Kim, Y.H. Xu, H.L. Zhu, Y.X. Qi, L.W. Yin, H. Li, N. Lun, Y. J. Bai, J. Power Sources 379 (2018) 270–277.
[21] H. Tang, Y. Zhou, L. Zan, N. Zhao, Z. Tang, Electrochim. Acta 191 (2016) 887–894.
[22] S. Wang, L. Wang, Z. Meng, B. Luo, RSC Adv. 8 (2018) 31628–31632.
[23] C. Chen, C. Ai, X. Liu, Y. Wu, Electrochim. Acta 227 (2017) 285–293.
[24] T.F. Yi, J.Z. Wu, J. Yuan, Y.R. Zhu, P.F. Wang, ACS Sustain. Chem. Eng. 3 (2015) 3062–3069.
[25] H. Li, Z. Li, X. Liang, J. Ouyang, Y. Ma, Y. Cui, C. Ma, Z. Tang, Mater. Lett. 192 (2017) 128–132.
[26] F. Qie, Z. Tang, Mater. Express 4 (2014) 221–227.
[27] S. Wang, Y. Bi, L. Wang, Z. Meng, B. Luo, Electrochim. Acta 301 (2019) 319–324.
[28] H. Tang, Z. Tang, C. Du, F. Qie, J. Zhu, Electrochim. Acta 120 (2014) 187–192.
[29] C. Chen, C. Ai, X. Liu, Electrochim. Acta 265 (2018) 448–454.
[30] B. Tian, H. Xiang, L. Zhang, Z. Li, H. Wang, Electrochim. Acta 55 (2010) 5453–5458.
[31] W. Chen, H. Liang, W. Ren, L. Shao, J. Shu, Z. Wang, J. Alloys Compd. 611 (2014) 65–73.
[32] Y. Li, C. Du, J. Liu, F. Zhang, Q. Xu, D. Qu, X. Zhang, Z. Tang, Electrochim. Acta 167 (2015) 201–206.
[33] H. Tang, J. Zhu, Z. Tang, C. Ma, J. Electroanal. Chem. 731 (2014) 60–66.
[34] H. Tang, Z. Tang, J. Alloys Compd. 613 (2014) 267–274.
[35] S.B. Simonsen, T.T. Muhl, K.T.S. Thydén, C. Chatzichristodoulou, J. Nielsen, B. R. Sudireddy, Solid State Ionics 340 (2019), 115019.
[36] Z. Zhong, Electrochem. Solid State Lett. 10 (2007) A267–A269.
[37] T. Lan, H. Qiu, F. Xie, J. Yang, M. Wei, Sci. Rep. 5 (2015) 8498.
[38] T.F. Yi, Z.K. Fang, Y. Xie, Y.R. Zhu, S.Y. Yang, ACS Appl. Mater. Interfaces 6 (2014) 20205–20213.
[39] H. Li, Z. Li, Y. Cui, C. Ma, Z. Tang, New J. Chem. 41 (2017) 975–981.
[40] S. Bhuvaneswari, U. Varadaraju, R. Gopalan, R. Prakash, Electrochim. Acta 327 (2019), 135008.
[41] H. Sun, Y. Chen, C. Xu, D. Zhu, L. Huang, J. Solid State Electrochem. 16 (2012) 1247–1254.
[42] S. Bhuvaneswari, U. Varadaraju, R. Gopalan, R. Prakash, Electrochim. Acta 301 (2019) 342–351.
[43] A. Wei, W. Li, Q. Chang, X. Bai, R. He, L. Zhang, Z. Liu, Y. Wang, Electrochim. Acta 323 (2019), 134692.
[44] W. Chen, Z. Zhou, H. Liang, L. Shao, J. Shu, Z. Wang, J. Power Sources 281 (2015) 56–68.
[45] S.K. Singh, S.R. Kiran, V. Murthy, Mater. Chem. Phys. 141 (2013) 822–827.
[46] C. Julien, M. Camacho-Lopez, Mater. Sci. Eng. B 108 (2004) 179–186.
[47] H. Song, S.-W. Yun, H.-H. Chun, M.-G. Kim, K.Y. Chung, H.S. Kim, B.-W. Cho, Y.-T. Kim, Energy Environ. Sci. 5 (2012) 9903–9913.
[48] Y. Ge, H. Jiang, K. Fu, C. Zhang, J. Zhu, C. Chen, Y. Lu, Y. Qiu, X. Zhang, J. Power Sources 272 (2014) 860–865.
[49] T. Senda, R.C. Bradt, J. Am. Ceram. Soc. 74 (1991) 1296–1302.
[50] J. Mao, K. Dai, M. Xuan, G. Shao, R. Qiao, W. Yang, V.S. Battaglia, G. Liu, ACS Appl. Mater. Interfaces 8 (2016) 9116–9124.
[51] L. Yang, X. Zhang, Y. Li, F. Hao, H. Chen, M. Yang, D. Fang, Electrochim. Acta 155 (2015) 272–278.
[52] W. Chen, H. Liang, L. Shao, J. Shu, Z. Wang, Electrochim. Acta 152 (2015) 187–194.
[53] X. Li, L. Qiao, D. Li, X. Wang, W. Xie, D. He, J. Mater. Chem. 1 (2013) 6400–6406.
[54] J. Guo, F. Li, J. Sui, H. Zhu, X. Zhang, Ionics 20 (2014) 1635–1639.
[55] L. Wang, Q. Xiao, Z. Li, G. Lei, L. Wu, P. Zhang, J. Mao, Electrochim. Acta 77 (2012) 77–82.
[56] B. Wang, J. Wang, J. Cao, H. Ge, Y. Tang, J. Power Sources 266 (2014) 150–154.
[57] K. Shaju, G.S. Rao, B. Chowdari, J. Mater. Chem. 13 (2003) 106–113.
[58] Y. Shi, L. Wen, F. Li, H.-M. Cheng, J. Power Sources 196 (2011) 8610–8617.
[59] B. Li, C. Han, Y.-B. He, C. Yang, H. Du, Q.-H. Yang, F. Kang, Energy Environ. Sci. 5 (2012) 9595–9602.